Available online at www.sciencedirect.com
ScienceDirect
Trans. Nonferrous Met. Soc. China 34(2024) 3615−3628
Transactions of Nonferrous Metals Society of China
www.tnmsc.cn

Microstructural evolution and hot tensile behavior of Mg−3Zn−0.5Zr alloy subjected to multi-pass friction stir processing

Ji WANG[1,2], Rui-dong FU[1,3], Tian-xiang HU[4], Yi-jun LI[1,3], Yue LIU[1], Zhi-hua ZHU[2], Shi-de LI[2], Zhe-feng XU[1,3]

1. State Key Laboratory of Metastable Materials Science and Technology, Yanshan University, Qinhuangdao 066004, China;
2. CITIC Dicastal Co., Ltd., Qinhuangdao 066004, China;
3. College of Materials Science and Engineering, Yanshan University, Qinhuangdao 066004, China;
4. Capital Aerospace Machinery Co., Ltd., Beijing 100076, China

Received 21 February 2024; accepted 3 September 2024

Abstract: The microstructures and hot tensile behaviors of ZK30 alloys subjected to single- and multi-pass friction stir processing (FSP) were systematically investigated. Following single-pass FSP (S-FSP), coarse grains underwent refinement to 1−2 μm, with a distinct basal texture emerging in the stir zone (SZ). Additionally, second-phase particles were fragmented, dispersed, and partially dissolved. Multi-pass FSP (M-FSP) further enhanced the homogeneity of the microstructure, reduced texture intensity differences, and decreased the fraction of second-phase particles by 50%. Both S-FSP and M-FSP SZs demonstrated superplasticity at strain rates below 1×10^{-3} s^{-1} and at temperatures of 250−350 °C. The S-FSP SZ exhibited an elongation of 390% at 250 °C and 1×10^{-4} s^{-1}, while the M-FSP SZ achieved an elongation of 406% at 350 °C and 1×10^{-3} s^{-1}. The superplastic deformation of SZ was co-dominated by grain boundary sliding (GBS) and the solute-drag mechanism in S-FSP and mainly by GBS in M-FSP.

Key words: ZK30 alloys; multi-pass friction stir processing; superplasticity; microstructure; hot tensile behavior

1 Introduction

Magnesium alloys, recognized for being the lightest structural metals, offer commendable specific strengths and modulus, excellent damping properties, abundant reserves, and ease of recycling [1−6]. Mg−Zn−Zr alloys, a prominent category among deformation magnesium alloys, demonstrate the capability to produce intricate large forgings [7−9]. However, the hexagonal close packing (HCP) crystal structure of Mg alloys makes them prone to cracking during plastic forming at room temperature [10]. In this context, hot deformation has emerged as an effective method to address the low formability of magnesium alloys [11−13]. A noteworthy tensile elongation of 470% in WE43 Mg alloy at a high temperature (375 °C) and a considerably low strain rate was reported [14]. Equal channel angular was employed to press on Mg alloys, and tensile elongations to fracture of 550% and 750% were achieved at temperatures of 200 and 250 °C, respectively, under a strain rate of 0.0001 s^{-1} [15]. In addition, the tensile behavior of the Mg−Al−Zn alloy has been investigated, noting an increase in elongation with elevated temperature and a decreased strain rate [16].

It is fundamental prerequisite of establishing a

Corresponding author: Rui-dong FU, Tel: +86-335-8074631, Fax: +86-335-8074545, E-mail: rdfu@ysu.edu.cn;
Yi-jun LI, Tel: +86-335-8387690, Fax: +86-335-8074545, E-mail: liyijun1987@ysu.edu.cn
DOI: 10.1016/S1003-6326(24)66629-X
1003-6326/© 2024 The Nonferrous Metals Society of China. Published by Elsevier Ltd & Science Press
This is an open access article under the CC BY-NC-ND license (http://creativecommons.org/licenses/by-nc-nd/4.0/)

uniform microstructure with fine grains [17], coupled with good thermal stability [18,19] for the high-temperature forming of magnesium alloys. Friction stir processing (FSP) stands out among the widely adopted techniques for modifying magnesium alloy microstructures [20,21]. For FSP technologies, the heat source is the friction of a special tool against the surface of the modified material, combined with strong plastic deformation. As a mature solid-state processing technique, FSP involves the interplay of temperature, mechanics, and metallurgy [22]. The severe plastic deformation and corresponding frictional and deformation heat contribute to solid-state and microstructural modification, effectively inhibiting the growth of recrystallized grains to achieve fine-grain microstructures [23]. Prior research has demonstrated that FSP significantly refines the grains of magnesium alloys, resulting in favorable hot tensile properties, including superplasticity [24−26]. For instance, AZ91 alloy processed by FSP exhibited an average grain size of 0.5 μm and an elongation rate of 1251% at a high strain rate of 1×10^{-2} s^{-1} [27]. Friction stir processed AZ91 alloy also displayed low-temperature superplasticity at 200 °C and 3×10^{-3} s^{-1}, with an elongation rate of 204% [28].

However, numerous investigations have highlighted the presence of microstructure inhomogeneity with regard to the temperature and strain gradients in the stir zone (SZ) following single-pass FSP (S-FSP) [29]. Consequently, multi-pass FSP (M-FSP) has consistently been employed to enhance the microstructure uniformity and mechanical performance [30−33]. In contrast to the widely studied ZK60 alloy in industrial applications, ZK30 (Mg−3Zn−0.5Zr) alloy offers the advantage of reduced metallurgical expenses. However, owing to its lower zinc content, ZK30 exhibits decreased strength and plasticity compared to ZK60, which makes it susceptible to cracking during plastic forming and limits its practical utility. Despite its potential for widespread use in automotive manufacturing, there is few study focusing on the microstructural evolution and mechanical behaviors at elevated temperatures in ZK30 alloy after S-FSP or M-FSP. This study delves into the microstructural changes in ZK30 following both S-FSP and M-FSP and investigates the hot tensile behavior of the SZ at varying temperatures. Additionally, the deformation mechanism is elucidated in detail.

2 Experimental

The ZK30 alloy employed in this study originated as a semi-continuous casting ingot and underwent subsequent hot extrusion and homogenization treatment processes. Figure 1 reveals an initial ZK30 alloy microstructure consisting primarily of an equiaxed α-Mg matrix and $MgZn_2$ second phase distributed along grain boundaries [34].

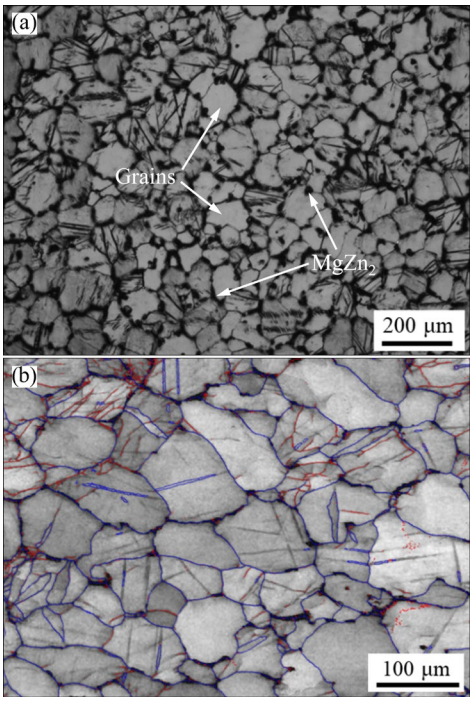

Fig. 1 Microstructure of ZK30 magnesium alloy base material: (a) Optical microscopy image; (b) EBSD image of grain boundary

A 4 mm-thick plate was friction stir processed using the FSW-3LM−2010 equipment, employing an H13 steel stirring tool with a shoulder diameter of 12 mm and a conical-shaped (3.5−3 mm) stirring pin with a length of 3 mm. The inclination angle of the stirring tool was set at 2.5°, the reduction was 0.2 mm, and the processing preheating time was 10 s. The FSP parameters were configured at 800 r/min and 200 mm/min for both one pass (referred to as S-FSP) and three passes (referred to as M-FSP). The termination position of the preceding pass served as the starting position for the subsequent pass, without any significant time gap, ensuring a pass overlap rate of 100%.

For microstructural examinations, specimens were cross-sectioned perpendicular to the FSP

direction. Microstructural characterization and analysis involved optical microscopy (OM), electron backscatter diffraction (EBSD), and scanning electron microscopy (SEM). Specimens for OM and SEM underwent preparation through mechanical polishing and etching with a solution of 5 vol.% HNO_3 and 95 vol.% ethanol. EBSD specimens were prepared through mechanical polishing and electropolishing (40 vol.% H_3PO_4 and 60 vol.% ethanol at 20 °C) at a voltage of 2−3 V for 10−20 s. The grain size measurements of the EBSD specimens were performed using OIM Analysis 7.3.1 software based on ASM International [35]. Particle volume fractions were determined using Image-Pro Plus 6.0 software.

Hardness measurements were conducted using a Vickers microhardness testing machine with a 100 g load and a 10 s dwell time at points distanced 0.5 mm from the top surface to a depth of 3.5 mm on the cross-section of the SZ.

Tensile tests were carried out according to ISO 6892-2:2018. Due to the size limitation of the SZ, the tensile specimens were proportionally scaled down with a gauge length, width, and thickness of 5, 3.5, and 1.5 mm, respectively, and machined along the processing direction at the SZ. The tests were performed utilizing a RDL50 high-temperature tensile tester for both S-FSP and M-FSP. The temperatures for the tensile tests were set at 250, 300, and 350 °C, with strain rates of 1×10^{-2}, 1×10^{-3}, and 1×10^{-4} s^{-1}. Tensile specimens were allowed to equilibrate at the set tensile temperature for 10 min before testing. Furthermore, the fracture surfaces were examined using SEM.

3 Results

3.1 Microstructure of SZ in S-FSP and M-FSP

The macroscopic morphology of the SZ cross-sections perpendicular to the processing direction after various processing passes is depicted in Fig. 2. The SZ exhibits well-formed structures free of defects such as pores or tunnels. With increase of pass, the width at the middle of the SZ slightly increases, which is attributed to the metal flow in M-FSP.

Grain boundary maps of the SZ under various processing passes are illustrated in Fig. 3. The blue lines denote grain boundaries exceeding 15°, while the red lines represent boundaries ranging from 2° to 15°. Compared to those in the base material (BM), the grains in the processed area are substantially refined. Notably, an evident inhomogeneity in grain size is observed between the upper and lower sections of the S-FSP SZ (Figs. 3(a, b). Furthermore, S-FSP results in finer grains with a banded distribution. With an increase in the number of passes, the average grain size increases slightly, and the grain size inhomogeneity between the upper and lower sections of the SZ decreases (Figs. 3(c, d)).

The misorientation angle statistics of grain boundaries in the SZ are presented in Fig. 4. Misorientation angles below 5° were excluded to minimize noise impact. Peaks at 30° and 90° are frequently associated with twinning [36]. In contrast to the BM, the entire SZ exhibits a high proportion of high-angle grain boundaries (above 15°). As the number of pass increases, the distribution of misorientation angles gradually aligns with that of the BM, especially with a reduction in peak intensity near 30° and a rightward shift of the peak near 90°.

SEM images of the second phase in the SZ for various numbers of processing passes are displayed in Fig. 5. Through FSP, the coarse second-phase particles along the grain boundaries in the BM are fragmented and dispersed. The area fractions of the

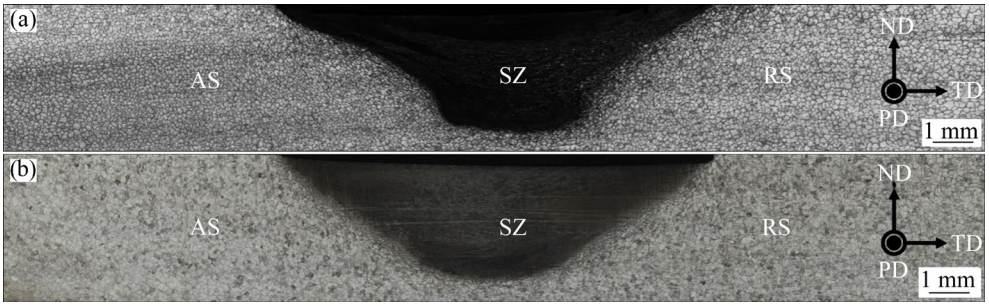

Fig. 2 Macroscopic morphology of cross-section of processed area: (a) S-FSP; (b) M-FSP

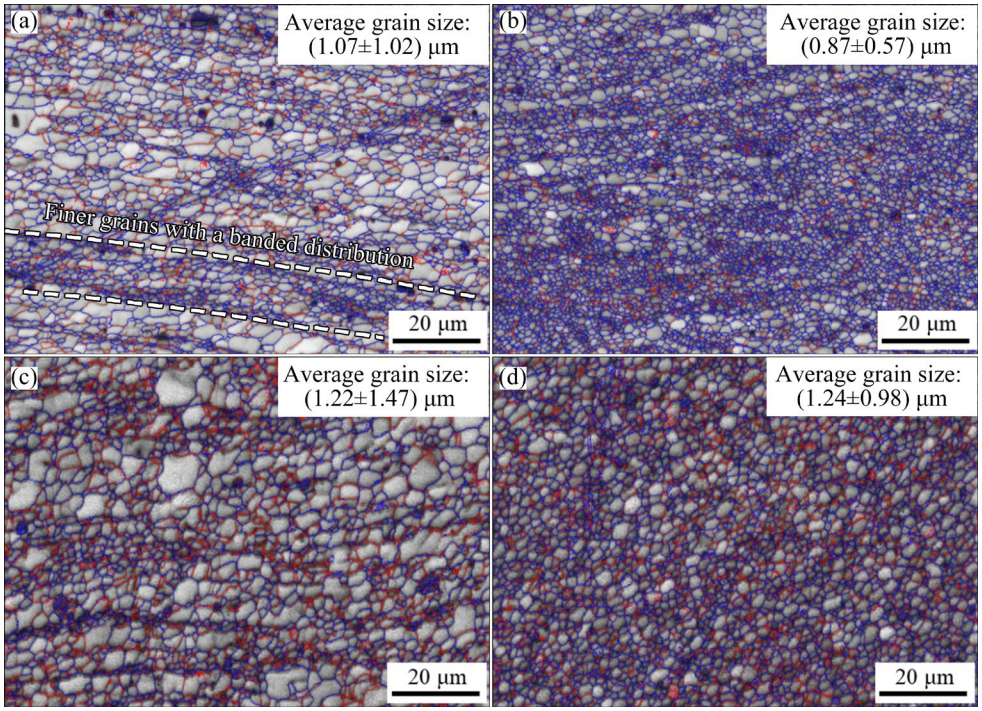

Fig. 3 Grain boundary EBSD maps of SZ: (a) Upper section of S-FSP SZ; (b) Lower section of S-FSP SZ; (c) Upper section of M-FSP SZ; (d) Lower section of M-FSP SZ

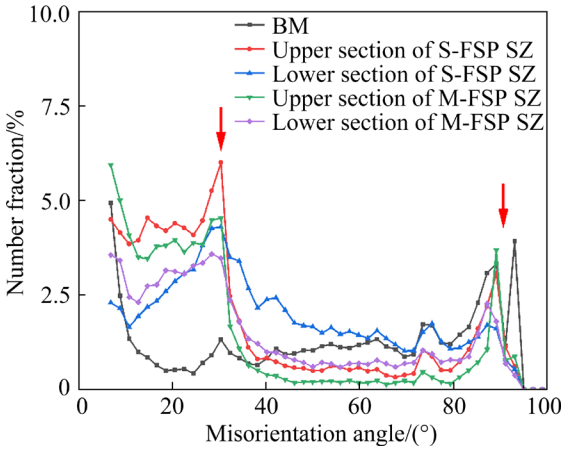

Fig. 4 Grain boundary misorientation distribution in SZ

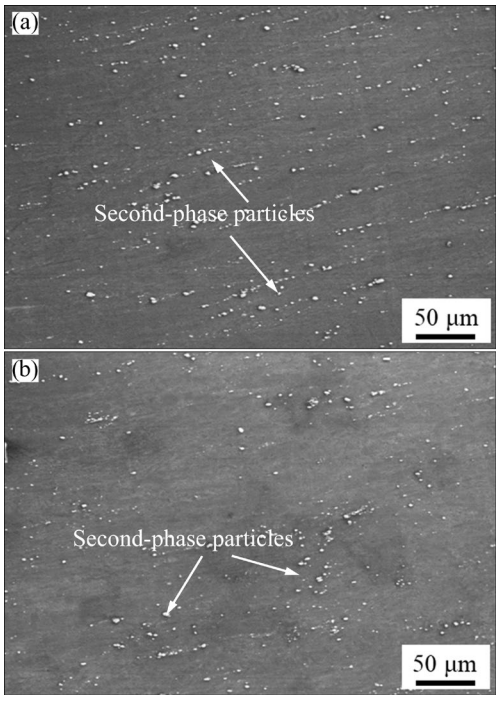

Fig. 5 Distribution of second-phase particles in SZ: (a) S-FSP SZ; (b) M-FSP SZ

second phase in the BM and in the S-FSP and M-FSP SZs were measured using Image-Pro Plus software. The fraction of second-phase particles in the BM was 2.79%, whereas in the S-FSP zone, it was reduced to 1.35%, which is only 48.39% of that in the BM. The fraction further decreased to 0.75% in the M-FSP zone, indicating the re-dissolving of the initial second-phase particles during FSP. An increase in the number of processing pass promotes this re-dissolving of the second-phase particles.

Pole figures of {0002}, $\{10\bar{1}1\}$, $\{10\bar{1}0\}$ and $\{10\bar{1}2\}$ for the BM and SZs under S-FSP and M-FSP are depicted in Fig. 6. The texture of the BM is randomly distributed, with a maximum intensity of only 5.56. After FSP, a strong grain orientation distribution in the ⟨0002⟩ direction, parallel to the processing direction, is formed in both the S-FSP and M-FSP SZs. Additionally, the texture intensity in the upper section is greater than that in the

lower section of the SZs under both processing conditions. Moreover, the difference in texture intensity decreases with an increase in the number of pass.

3.2 Microhardness of SZ in S-FSP and M-FSP

Figure 7 shows the microhardness distribution across the cross-sections of the samples subjected to S-FSP and M-FSP. Notably, the S-FSP sample exhibits a significantly inhomogeneous microhardness distribution in Fig. 7(a). In contrast, after M-FSP, the microhardness distribution becomes homogenous, accompanied by a decrease in hardness. This reduction is attributed to grain growth and the re-dissolving of second-phase particles during M-FSP.

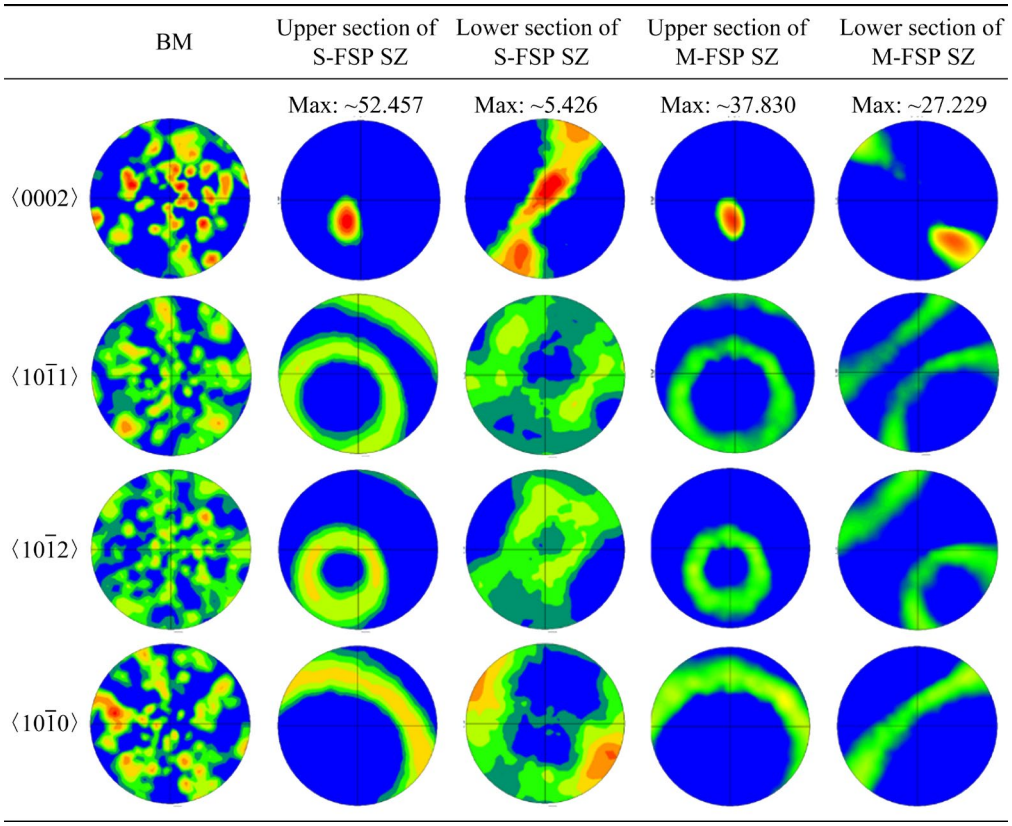

Fig. 6 Texture distribution in SZ

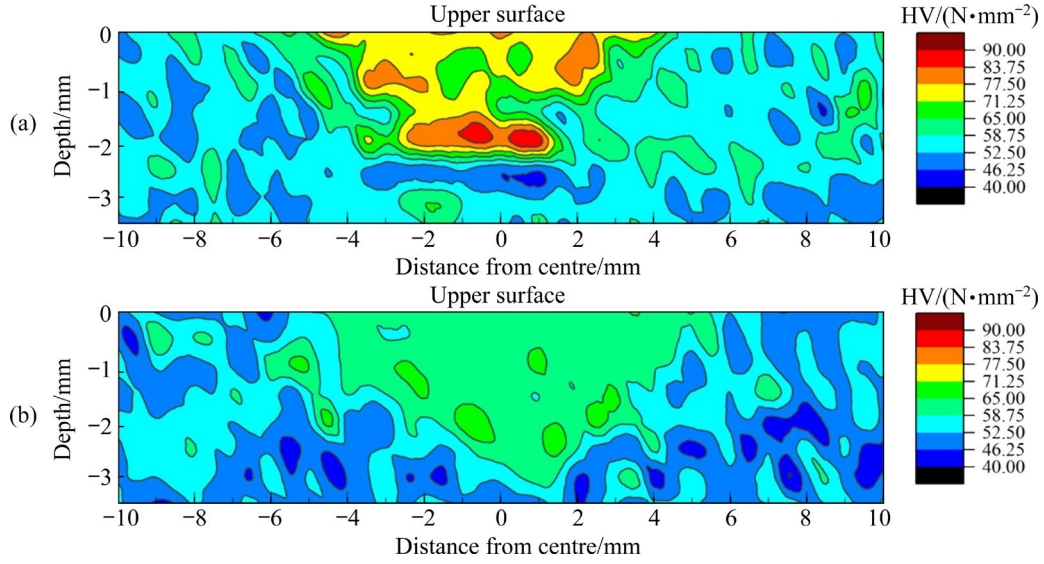

Fig. 7 Microhardness distribution in S-FSP (a) and M-FSP (b) SZs

3.3 Hot tensile performance of SZ in S-FSP and M-FSP samples

Figure 8 shows the tensile stress–strain curves of the SZ under different processing passes. Tables 1 and 2 present the tensile fractured samples and corresponding elongations for the S-FSP and M-FSP SZs at various temperatures and strain rates.

With an increase in temperature or a decrease in strain rate, the S-FSP and M-FSP SZs both exhibit an increase in elongation. At 250 °C, the elongation of the S-FSP SZ surpasses that of the M-FSP SZ. However, as the temperature reaches 300 °C or above (i.e., approaches or exceeds $0.5T_m$), the elongation of the M-FSP SZ consistently exceeds that of the S-FSP SZ. For the S-FSP SZ, at strain rates of 1×10^{-2} and 1×10^{-3} s^{-1}, the elongation increases with an increase in deformation temperature. However, at 1×10^{-4} s^{-1}, elongation decreases with respect to temperature. Regarding the M-FSP SZ, the elongation generally exhibits an increase with temperature and a decrease with strain rate. However, at 350 °C and a strain rate of 1×10^{-4} s^{-1}, the elongation decreases to 198%, which is possibly related to the thermal stability of the microstructure.

3.4 Fracture morphology of hot tensile samples

Figure 9 depicts the typical fracture morphologies of the SZs of hot tensile samples subjected to S-FSP and M-FSP. The images reveal the presence of cleavage planes and some cavities in the S-FSP samples, along with numerous cavities in the M-FSP samples, potentially nucleating at the triple junctions of grain boundaries [36]. This phenomenon is recognized as a typical ductile fracture characterized by the coalescence of micropores, indicating that the formation and growth of such cavities are key factors influencing the failure process under hot tensile conditions.

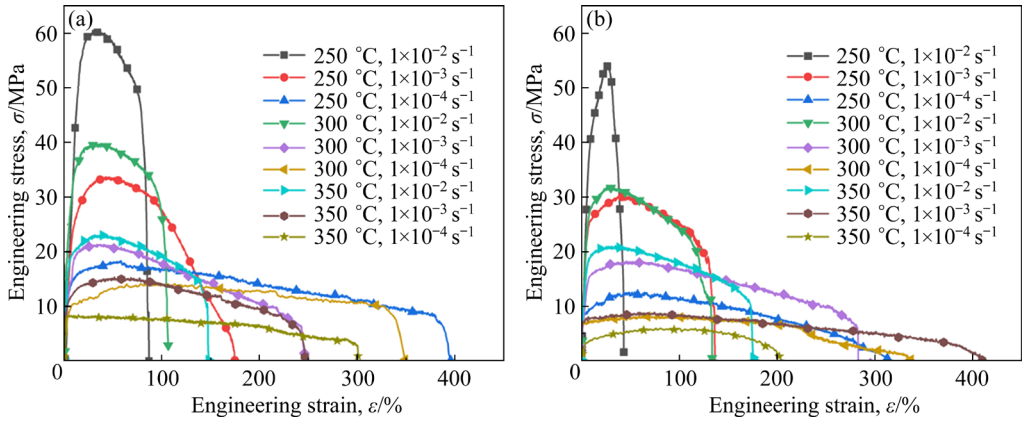

Fig. 8 Tensile stress–strain curves of SZ: (a) S-FSP; (b) M-FSP

Table 1 Hot tensile results of S-FSP SZ

No.	Strain rate/s^{-1}	Temperature/°C	Yield strength/MPa	Elongation to fracture/%	Tensile specimen
1	0.01	250	25.18	86	
2	0.01	300	15.94	92	
3	0.01	350	12.89	148	
4	0.001	250	13.02	172	
5	0.001	300	8.27	222	
6	0.001	350	7.73	239	
7	0.0001	250	6.88	390	
8	0.0001	300	5.01	322	
9	0.0001	350	3.82	294	

Table 2 Hot tensile results of M-FSP SZ

No.	Strain rate/s^{-1}	Temperature/°C	Yield Strength/MPa	Elongation to fracture/%	Tensile specimen
1	0.01	250	21.76	42	
2	0.01	300	14.02	132	
3	0.01	350	8.99	166	
4	0.001	250	9.31	136	
5	0.001	300	7.48	264	
6	0.001	350	6.05	406	
7	0.0001	250	6.37	310	
8	0.0001	300	4.87	338	
9	0.0001	350	2.81	198	

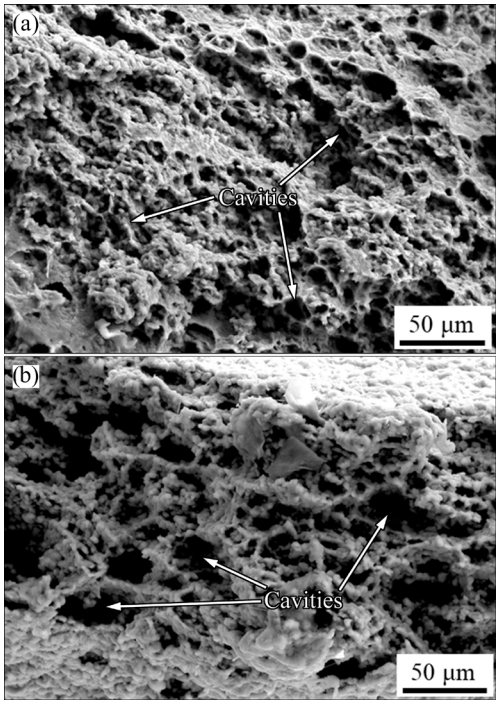

Fig. 9 SEM images of hot tensile fracture surfaces: (a) S-FSP SZ at 250 °C and 1×10^{-4} s^{-1}; (b) M-FSP SZ at 350 °C and $1\times10^{-3}s^{-1}$

4 Discussion

4.1 Effect of number of FSP pass on micro-structure evolution of SZ

The OM results indicate that FSP effectively refines the grains of the BM through dynamic recrystallization (DRX) [37,38]. However, in the case of the S-FSP SZ, the nonuniformity in grain size between the upper and low sections implies incomplete metal flow, particularly under the shoulder section. This results in the formation of banded regions comprising finer grains. According to the previous investigation [39], even after multiple processing passes with 100% overlap during M-FSP, further grain refinement becomes difficult. Theoretically, the grain size should remain the same after multiple passes since the same parameters are used during M-FSP. However, a slight grain growth was observed in the M-FSP SZ in this study. The grain growth is attributed to the accumulated thermal input experienced by the sample and the occurrence of DRX with each FSP pass. Moreover, increased processing temperature and enhanced metal plastic flow during M-FSP resulted in more uniform grain size between the upper and lower sections, with few observed bands.

During FSP, the second-phase particles undergo processes such as fragmentation, re-dissolution, and dispersion with metal flow. Additionally, they play a role in pinning dislocation movement and inhibiting grain boundary migration, thereby impeding grain growth during dynamic microstructural evolution. The low diffusion rate of alloying elements contributes to the formation of a fine-grained supersaturated solid solution in the SZ. In contrast to S-FSP, the increasing temperature during M-FSP promotes the re-dissolution of second-phase particles. Concurrently, the material movement facilitates a more uniform distribution within the Mg matrix, thereby reducing the inhibitory pinning effect on grain growth. The variation in average microhardness aligns well with

the change in grain size and the distribution of second-phase particles in both the S-FSP and M-FSP SZs.

4.2 Effect of FSP pass on hot tensile and fracture behavior of SZ

As elucidated earlier, FSP is effective in refining the microstructure and enhancing mechanical properties. Corresponding with the results of hot tensile testing, both S-FSP and M-FSP SZs display increased elongation with rising temperatures or decreasing strain rates. Notably, certain S-FSP and M-FSP samples exhibit exceptional plastic deformation, particularly the S-FSP samples at a strain rate of 1×10^{-4} s^{-1} and temperature of 250 °C and M-FSP samples at a strain rate of 1×10^{-3} s^{-1} and temperature of 350 °C, demonstrating superplastic behavior with elongations of 390% and 406%, respectively.

The strain rate sensitivity (m-value), a metric for evaluating hot tensile flow behaviors, is calculated according to Eq. (1):

$$m=\frac{\partial \ln\sigma}{\partial \ln\dot{\varepsilon}} \tag{1}$$

where σ is the peak stress, and $\dot{\varepsilon}$ is the strain rate. Figure 10 illustrates the $\ln\sigma-\ln\dot{\varepsilon}$ plots at various deformation temperatures for S-FSP and M-FSP. The graphs reveal that the flow stress of the S-FSP and M-FSP SZs decreases with temperature at a constant strain rate and increases with strain rate at a constant temperature. Notably, at the same temperature and strain rate, the flow stress of S-FSP slightly exceeds that of M-FSP.

The m-values, represented by the slopes of the $\ln\sigma-\ln\dot{\varepsilon}$ lines obtained through linear fitting of the data points, indicate varying strain rate sensitivities. All the m-values decrease with increasing temperature. The m-values of the M-FSP samples are slightly higher than 0.3, whereas those of the S-FSP samples are not, suggesting that M-FSP enhances the elongation of the SZ at higher temperatures.

In this context, the Arrhenius equation [40] can be employed to explore the relationship among peak flow stress, strain rate, and temperature. The equation is expressed as follows:

$$\dot{\varepsilon}=A_1\sigma^{n_1} \tag{2}$$

$$\dot{\varepsilon}=A_2\exp(\beta\sigma) \tag{3}$$

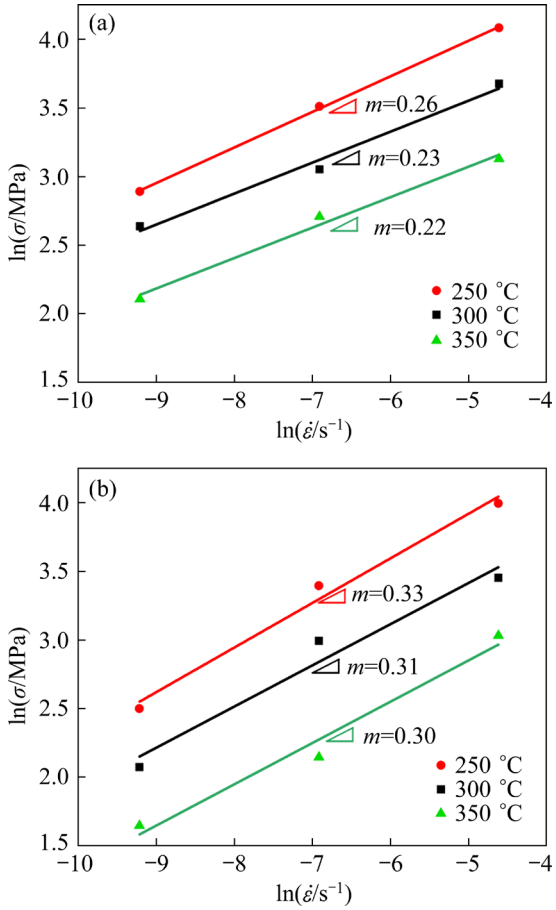

Fig. 10 $\ln\sigma-\ln\dot{\varepsilon}$ plots of hot tensile results: (a) S-FSP SZ; (b) M-FSP SZ

$$\dot{\varepsilon}=A[\sinh(\alpha\sigma)]^n\exp\left(\frac{-Q}{RT}\right) \tag{4}$$

By taking the logarithm of Eqs. (2) and (3), the material constants α=0.0461 and α=0.0597 for S-FSP and M-FSP, respectively, are calculated from the average values of n=4.2688 for S-FSP and n=3.29654 for M-FSP, alongside β=0.19682 for S-FSP and β=0.196963 for M-FSP, by the linear regression of $\ln\dot{\varepsilon}-\ln\sigma$ and $\ln\dot{\varepsilon}-\sigma$, as illustrated in Fig. 11.

Taking the natural logarithm of Eq. (4), we obtain

$$\ln\dot{\varepsilon}=\ln A-\frac{Q}{RT}+n\ln[\sinh(\alpha\sigma)] \tag{5}$$

The test data show a linear fitting relationship for $\ln\dot{\varepsilon}-\ln[\sinh(\alpha\sigma)]$, as illustrated in Figs. 12(a) and (b). Moreover, the activation energy (Q) can be expressed and calculated as follows:

$$Q=R\left.\frac{\partial\ln\dot{\varepsilon}}{\partial\ln[\sinh(\alpha\sigma)]}\right|_T\cdot\left.\frac{\partial\ln[\sinh(\alpha\sigma)]}{\partial(1000/T)}\right|_{\dot{\varepsilon}} \tag{6}$$

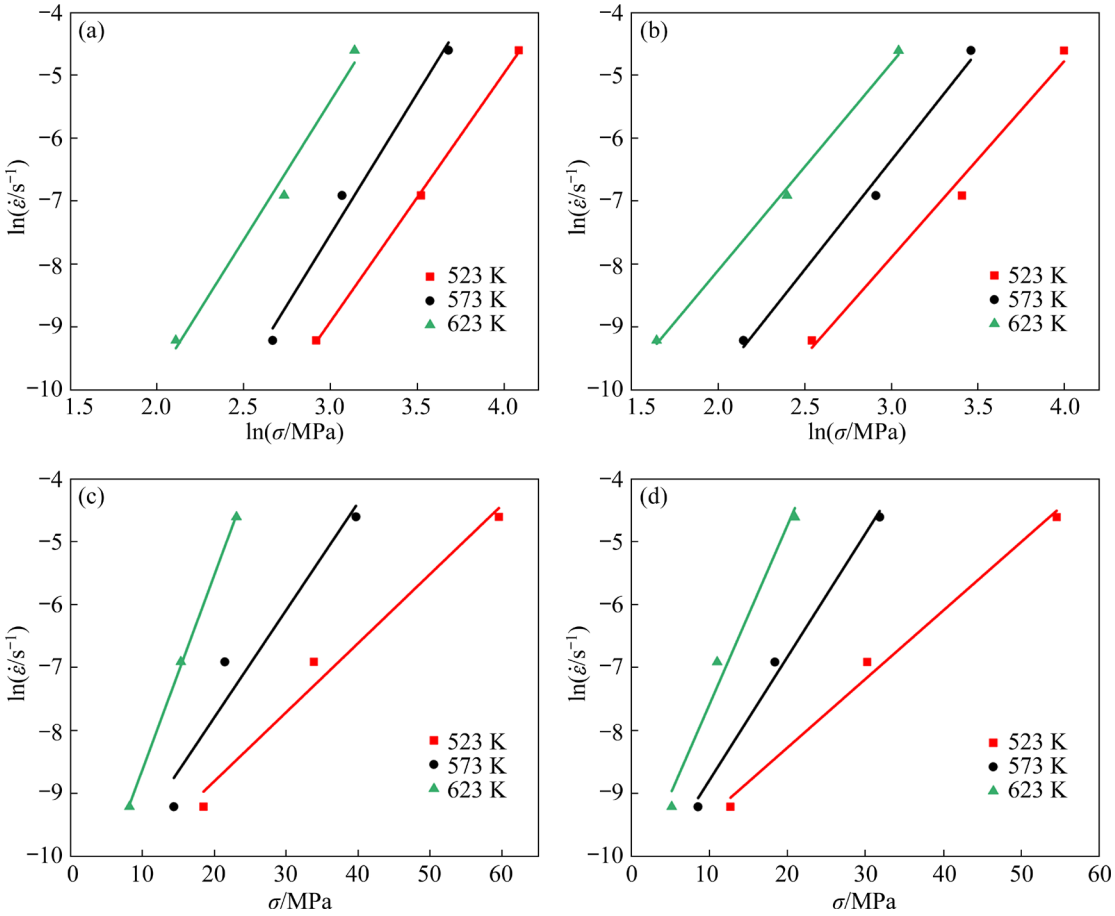

Fig. 11 $\ln \dot{\varepsilon} - \ln \sigma$ (a, b) and $\ln \dot{\varepsilon} - \sigma$ (c, d) plots of hot tensile results: (a, c) S-FSP SZ; (b, d) M-FSP SZ

By calculating the slope of the linear fit of the experimental data, we obtain Q=103.6 kJ/mol for S-FSP and Q=95.48 kJ/mol for M-FSP, as depicted in Figs. 12(c) and (d). The activation energies for both S-FSP and M-FSP slightly exceed the grain boundary diffusion activation energy (~90 kJ/mol) but are lower than the lattice diffusion activation energy (~135 kJ/mol). Notably, the activation energy of S-FSP is greater than that of M-FSP, which is attributed to a high volume of precipitates and twinning-induced deformation in the early stage [41].

Superplasticity has been reported under conditions of both low and high strain rates at low and high temperatures, with solute-drag creep (a dislocation creep mechanism) and grain boundary sliding (GBS) identified as dominant deformation mechanisms [42]. In general entailing a fine grain size (below 15 μm), a uniform microstructure, and high strain rate sensitivity (m>0.3), the primary deformation mechanism is GBS. Conversely, when the m-value is smaller than 0.3, solute-drag creep is the dominant deformation mechanism. In this study, despite the grain size being below 3 μm and M-FSP enhancing the homogeneity of the microstructure, GBS alone cannot attain high elongation in friction stir processed Mg alloys. The occurrence of GBS introduces stress concentration at crossed grain boundaries, subsequently inhibiting GBS and leading to pore formation. Therefore, for S-FSP, the superplastic deformation is jointly governed by GBS and the solute-drag creep mechanism [43]. As discussed in Section 4.1, during FSP, the low diffusion rate of alloying elements contributes to the formation of a fine-grained supersaturated solid solution in the SZ. A previous study [44] also indicated that solute atoms may preferentially segregate around dislocations during deformation at elevated temperatures, causing a drag force that interacts with moving dislocations. Therefore, GBS and solute-drag creep are primarily responsible for the tensile deformation observed in this study. Conversely, in the case of M-FSP, a thorough analysis of activation energy and the m-value suggests a relatively significant contribution from GBS.

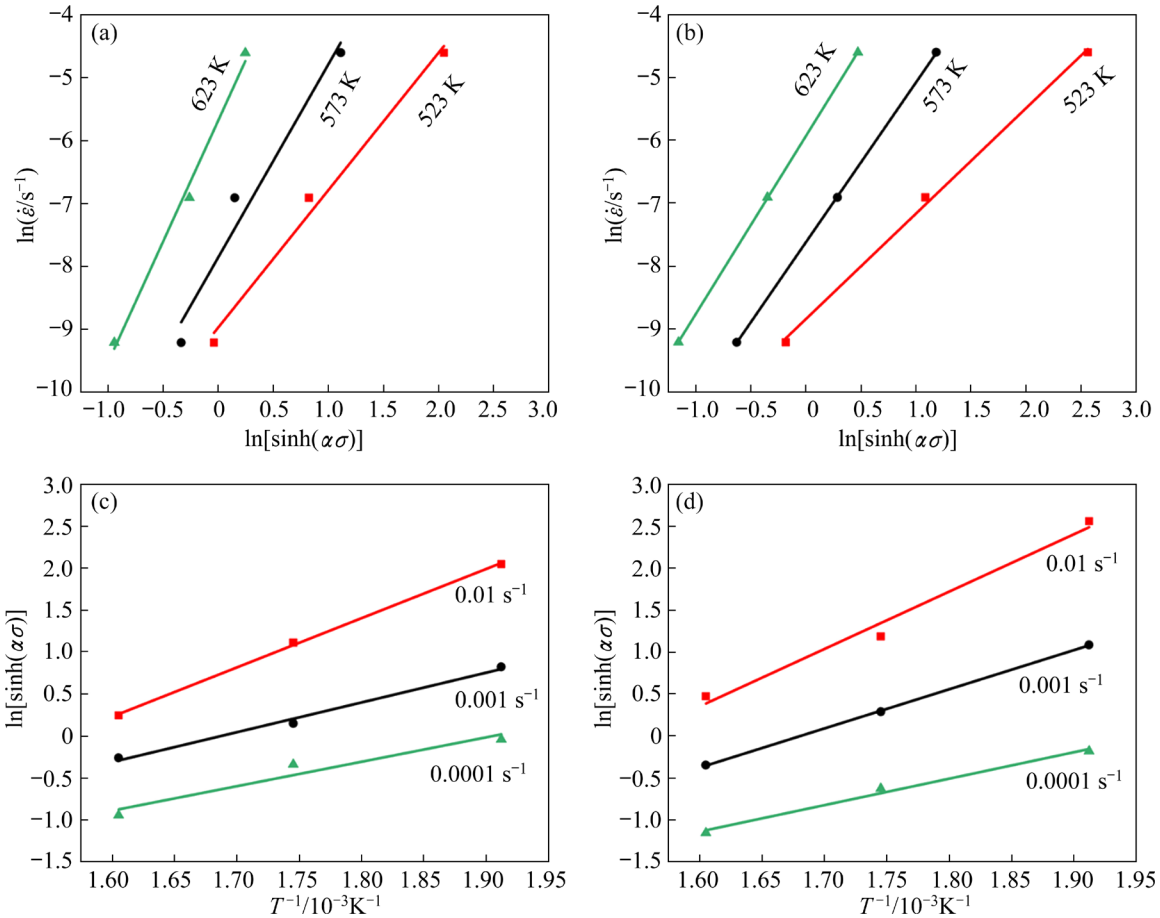

Fig. 12 $\ln\dot{\varepsilon}-\ln[\sinh(\alpha\sigma)]$ (a, b) and $\ln[\sinh(\alpha\sigma)]-T^{-1}$ (c, d) plots of hot tensile results: (a, c) S-FSP SZ; (b, d) M-FSP SZ

The layered flow of material around the rotating tool in S-FSP creates stacked shear layers, altering the grain orientation and forming a texture. M-FSP results in a noticeable modification of texture, which is tilted toward the processing and transverse directions, especially in the lower section. In addition, the texture is more uniform in the M-FSP SZ. The average Schmid factor values for $\{0001\}\langle\bar{1}1\bar{2}0\rangle$ in the friction stir processed samples are listed in Table 2. It demonstrates that the texture is advantageous for activating basal slips at the initial stage of the tensile test in both S-FSP and M-FSP. A more uniform texture in the SZ contributes further to the coordinated deformation.

Table 2 Average Schmid factor values for $\{0001\}\langle\bar{1}1\bar{2}0\rangle$ in S-FSP and M-FSP

S-FSP		M-FSP	
Upper section	Lower section	Upper section	Lower section
0.42	0.31	0.36	0.31

Additionally, during hot tensile deformation, other slip systems such as $\langle c+a\rangle$ are activated, which weakens the texture intensity. This weakening of the texture promotes the GBS phenomenon [28].

Furthermore, the second-phase particles substantially influence the thermal stability of the microstructure. In particular, they resist grain recrystallization and provide a Zener pinning effect at elevated temperatures. As the temperature increases and strain rates decrease, the increased dissolution and dispersion of second-phase particles in the M-FSP SZ weaken the pinning effect. This results in grain coarsening and decreased elongation during prolonged exposure to high temperatures. Figure 13 illustrates the microstructure near the fracture location after the stretching of the M-FSP SZ to failure at a strain rate of 1×10^{-4} s^{-1} and temperatures of 250, 300, and 350 °C. Under all conditions, the grains near the fracture locations maintain a uniformly distributed and equiaxed structure without elongation in the load direction. While grain growth is not prominent at 250 and

300 °C, it becomes more significant at 350 °C, exceeding 10 μm and consequently reducing the elongation (198%) of the M-FSP SZ.

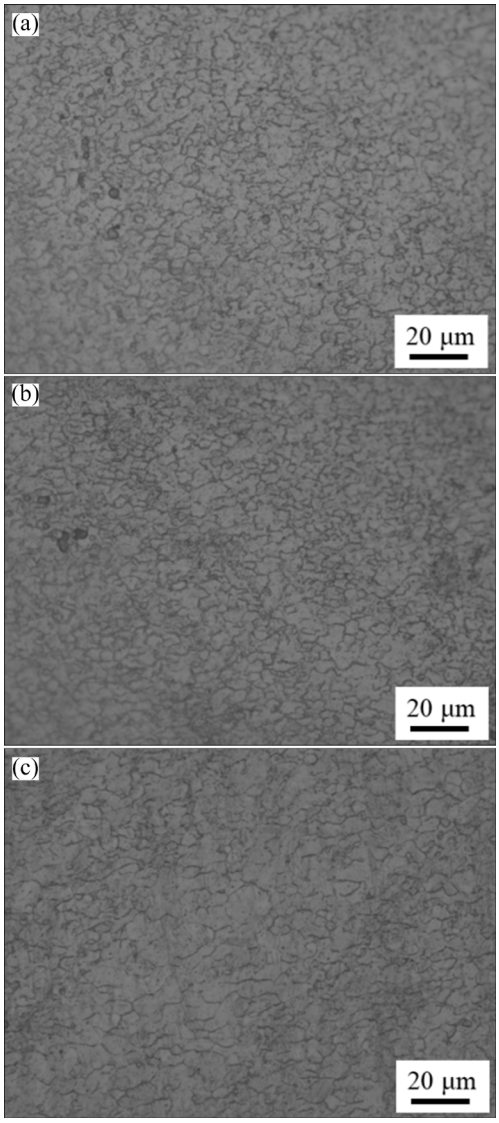

Fig. 13 Microstructures near fracture surface of M-FSP SZ at strain rate of 1×10^{-4} s^{-1}: (a) 250 °C; (b) 300 °C; (c) 350 °C

It is widely acknowledged that achieving higher elongation at elevated temperatures requires a fine grain size, uniform microstructure, high strain rate sensitivity (*m*-value), and thermal stability. Fracture behavior can reflect the mechanical performance. Figure 14 presents the microstructure near the fracture location in the S-FSP and M-FSP samples at 1×10^{-3} s^{-1} and 350 °C. It is evident that cavities preferentially form at grain boundaries. In regions where coarse and fine grains intersect, stress concentration is likely to occur, creating potential sites for cavity formation during hot deformation. Furthermore, as strain increases, the growth and merging of these cavities, coupled with uneven grain growth, may lead to tensile failure and intergranular fracture, impacting the total elongation of the SZ.

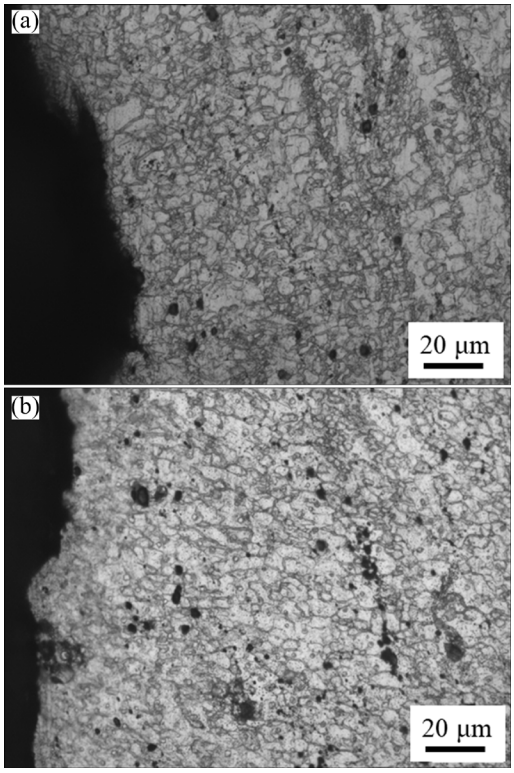

Fig. 14 Microstructures near fracture surfaces in SZs at 350 °C and 1×10^{-3} s^{-1}: (a) S-FSP SZ; (b) M-FSP SZ

5 Conclusions

(1) Compared to S-FSP, M-FSP enhances the homogeneity of the microstructure in the SZ, increases the average grain size to 1−1.3 μm, and improves the dissolution proportion of the second-phase particles by 50% while enabling a more dispersed distribution, and unifies the texture of the SZ.

(2) The SZs of both S-FSP and M-FSP samples exhibit superplasticity under suitable deformation conditions. The maximum elongation achieved by S-FSP is 390% at 250 °C and 1×10^{-4} s^{-1}, while for M-FSP, it reaches 406% at 350 °C and 1×10^{-3} s^{-1}.

(3) The superplastic deformation of the SZ is co-dominated by GBS and the solute-drag creep mechanism for S-FSP and mainly by GBS for M-FSP. At excessively high deformation temperatures (~350 °C) and low strain rates (~1×10^{-4} s^{-1}), grains in the SZ of M-FSP samples

undergo abnormal growth due to the decreased thermal stability of the microstructure, resulting in premature failure during high-temperature plastic deformation.

CRediT authorship contribution statement

Ji WANG: Conceptualization, Methodology, Formal analysis, Investigation, Data curation, Writing – Original draft, Visualization; **Rui-dong FU:** Conceptualization, Resources, Writing – Review & editing, Supervision; **Tian-xiang HU:** Conceptualization, Formal analysis; **Yi-jun LI:** Conceptualization, Data curation, Writing – Review & editing; **Yue LIU:** Data curation; **Zhi-hua ZHU:** Investigation; **Shi-de LI:** Investigation; **Zhe-feng XU:** Conceptualization, Data curation.

Declaration of competing interest

The authors declare that they have no known competing financial interests or personal relationships that could have appeared to influence the work reported in this paper.

Acknowledgments

This study was supported by Hebei Natural Science Foundation, China (No. E2020203158), and Hebei Provincial Department of Human Resources and Social Security, China (No. E2020100006).

References

[1] LIU Zhan, NIE Jin-feng, ZHAO Yong-hao. Effect of deformation processing on microstructure evolution and mechanical properties of Mg−Li alloys: A review [J]. Transactions of Nonferrous Metals Society of China, 2024, 34(1): 1−25.

[2] MALIK A, WANG Yang-wei, CHENG Huan-wu, NAZEER F, KHAN M A. Microstructure evolution of Mg−Zn−Zr magnesium alloy against soft steel core projectile [J]. Journal of Materials Science & Technology, 2021, 79: 46−61.

[3] BAYAT-TORK N, MAHMUDI R, HOSEINI-ATHAR M M. Hot deformation constitutive analysis and processing maps of extruded Mg−Gd binary alloys [J]. Journal of Materials Research and Technology, 2020, 9(6): 15346−15359.

[4] MA Ying-zhong, WANG De-xin, LI Hong-xiang, YANG Chang-lin, YUAN Fu-song, ZHANG Ji-shan. Microstructure, mechanical properties and corrosion behavior of quaternary Mg−1Zn−0.2Ca−*x*Ag alloy wires applied as degradable anastomotic nails [J]. Transactions of Nonferrous Metals Society of China, 2021, 31(1): 111−124.

[5] SU Ning, WU Yujuan, DENG Qing-chen, CHANG Zhi-yu, WU Qian-ye, XUE Yan-ting, YANG Kun, CHEN Qiang, PENG Li-ming. Synergic effects of Gd and Y contents on the age-hardening response and elevated-temperature mechanical properties of extruded Mg−Gd(−Y)−Zn−Mn alloys [J]. Materials Science and Engineering A, 2021, 810: 141019.

[6] MALIK A, WANG Yang-wei, NAZEER F. The development of a strong and ductile Mg−Zn−Zr thin sheet through nano precipitates and pre-induced dislocation [J]. Materials Science and Engineering A, 2021, 817: 141339.

[7] FAKHAR N, SABBAGHIAN M. A good combination of ductility, strength, and corrosion resistance of fine-grained ZK60 magnesium alloy produced by repeated upsetting process for biodegradable applications [J]. Journal of Alloys and Compounds, 2021, 862: 158334.

[8] LIANG Jing-wei, LEI Zheng-long, CHEN Yan-bin, WU Shi-bo, CHEN Xi, JIANG Meng, CAO Shi-yu , Formability, microstructure, and thermal crack characteristics of selective laser melting of ZK60 magnesium alloy [J]. Materials Science and Engineering A, 2022, 839: 142858.

[9] WANG Xue-yi, YANG Jun, CHI Pei-zhou, BAHONAR E, TAYEBI M. Effects of the microstructure and precipitation hardening on the thermal expansion behavior of ZK60 magnesium alloy [J]. Journal of Alloys and Compounds, 2022, 901: 163422.

[10] ZHANG Hua, REN Shuai, LI Xia, WANG Li-fei, FAN Jian-feng, CHEN Shu-ying, ZHU Li-long, MENG Fan-chao, TONG Yang, ROVEN H J, ZHANG Shang-zhou, JIANG Liang. Dramatically enhanced stamping formability of Mg−3Al−1Zn alloy by weakening (0001) basal texture [J]. Journal of Materials Research and Technology, 2020, 9(6): 14742−14753.

[11] FAKHAR N, SABBAGHIAN M. Hot shear deformation constitutive analysis of fine-grained ZK60 Mg alloy sheet fabricated via dual equal channel lateral extrusion and sheet extrusion [J]. Transactions of Nonferrous Metals Society of China, 2022, 32(8): 2541−2556.

[12] TAYLOR S, WEST G D, MOGIRE E, TANG F, KOTADIA H R. Superplastic forming characteristics of AZ41 magnesium alloy [J]. Transactions of Nonferrous Metals Society of China, 2021, 31(3): 648−654.

[13] GAN Yi, HU Li, SHI Lai-xin, CHEN Qiang, LI Ming-ao, XIANG Lin, ZHOU Tao. Effect of AlLi phase on deformation behavior and dynamic recrystallization of Mg−Li alloy during hot compression [J]. Transactions of Nonferrous Metals Society of China, 2023, 33(5): 1373−1384.

[14] KANDALAM S, SABAT R K, BIBHANSHU N, AVADHANI G S, KUMAR S, SUWAS S. Superplasticity in high temperature magnesium alloy WE43 [J]. Materials Science and Engineering A, 2017, 687: 85−92.

[15] FIGUEIREDO R B, LANGDON T G. Achieving superplastic properties in a ZK10 magnesium alloy processed by equal-channel angular pressing [J]. Journal of Materials Research and Technology, 2017, 6(2): 129−135.

[16] KIM W J, PARK J D, YOON U S. Superplasticity and superplastic forming of Mg−Al−Zn alloy sheets fabricated by strip casting method [J]. Journal of Alloys and Compounds, 2008, 464(1/2): 197−204.

[17] VÁVRA T, MINÁRIK P, VESELÝ J, KRÁL R. Excellent superplastic properties achieved in Mg−4Y−3RE alloy in high strain rate regime [J]. Materials Science and

Engineering A, 2020, 784: 139314.

[18] MD F K, PANIGRAHI S K. Achieving excellent superplasticity in an ultrafine-grained QE22 alloy at both high strain rate and low-temperature regimes [J]. Journal of Alloys and Compounds, 2018, 747: 71−82.

[19] SUN Chao, LIU Huan, WANG Xiao-jun, HU Xiao-shi, JIANG Shao-song. Microstructure evolution during superplastic deformation process and its impact on superplastic behavior of a Mg−Gd−Y−Zn−Zr alloy [J]. Materials Characterization, 2021, 172: 110879.

[20] WANG Wen, HAN Peng, PENG Pai, ZHANG Ting, LIU Qiang, YUAN Sheng-nan, HUANG Li-ying , YU Hai-liang, QIAO Ke, WANG Kuai-she. Friction stir processing of magnesium alloys: A review [J]. Acta Metallurgica Sinica (English Letters), 2020, 33: 43−57.

[21] MISHRA R S, MA Z Y. Friction stir welding and processing [J]. Materials Science and Engineering: R: Reports, 2005, 50(1/2): 1−78.

[22] MENG Xiang-chen, HUANG Yong-xian, CAO Jian, SHEN Jun-jun, SANTOS J F. Recent progress on control strategies for inherent issues in friction stir welding [J]. Progress in Materials Science, 2021, 115: 100706.

[23] XIE Yu-ming, MENG Xiang-chen, LI Yu-long, MAO Dong-xin, WAN Long, HUANG Yong-xian. Insight into ultra-refined grains of aluminum matrix composites via deformation-driven metallurgy [J]. Composites Communications, 2021, 26: 100776.

[24] ZHANG Da-tong, XIONG Feng, ZHANG Wei-wen, QIU Cheng, ZHANG Wen. Superplasticity of AZ31 magnesium alloy prepared by friction stir processing [J]. Transactions of Nonferrous Metals Society of China, 2011, 21(9): 1911−1916.

[25] YANG Q, XIAO B L, MA Z Y, CHEN R S. Achieving high strain rate superplasticity in Mg−Zn−Y−Zr alloy produced by friction stir processing [J]. Scripta Materialia, 2011, 65(4): 335−338.

[26] XU Nan, REN Zi-ke, FAN Yue, GU Bo-kun, SHEN Jun, SONG Qi-ning, ZHAO Jian-hua, BAO Ye-feng. Microstructural evolution and mechanical properties of cooling medium assistant friction stir processed AZ31B Mg alloy [J]. Transactions of Nonferrous Metals Society of China, 2023, 33(6): 1729−1741.

[27] MOHAN A, YUAN W, MISHRA R S. High strain rate superplasticity in friction stir processed ultrafine grained Mg−Al−Zn alloys [J]. Materials Science and Engineering A, 2013, 562: 69−76.

[28] ZHANG Da-tong, WANG Sai-xiang, QIU Chen, ZHANG Wen. Superplastic tensile behavior of a fine-grained AZ91 magnesium alloy prepared by friction stir processing [J]. Materials Science and Engineering A, 2012, 556: 100−106.

[29] YUAN W, MISHRA R S, CARLSON B, MISHRA R K, VERMA R, KUBIC R. Effect of texture on the mechanical behavior of ultrafine grained magnesium alloy [J]. Scripta Materialia, 2011, 64(6): 580−583.

[30] EIVANI A R, MEHDIZADE M, CHABOK S, ZHOU J. Applying multi-pass friction stir processing to refine the microstructure and enhance the strength, ductility and corrosion resistance of WE43 magnesium alloy [J]. Journal of Materials Research and Technology, 2021, 12: 1946−1957.

[31] KUMAR A, GOTAWALA N, MISHRA S, SHRIVASTAVA A. Defects, microstructure and mechanical behaviour upon multi-pass friction stir processing of magnesium alloy with spiral tool path [J]. CIRP Journal of Manufacturing Science and Technology, 2021, 32: 170−178.

[32] LUO X C, ZHANG D T, CAO G H, QIU C, CHEN D L. High-temperature tensile behavior of AZ61 magnesium plate prepared by multi-pass friction stir processing [J]. Materials Science and Engineering A, 2019, 759: 234−240.

[33] LUO X C, ZHANG D T, ZHANG W W, QIU C, CHEN D L. Tensile properties of AZ61 magnesium alloy produced by multi-pass friction stir processing: Effect of sample orientation [J]. Materials Science and Engineering A, 2018, 725: 398−405.

[34] YANG Chu-bin, ZHANG Zhen, JIANG Xin-yi, LIN Xi, LUO Ning, HAN Bao-jun, ZHANG Xiao-lian. Comparison of the thermal conductivity of Sm-containing AZ31 and ZK30 alloys [J]. International Journal of Thermophysics, 2019, 40: 81.

[35] VOORT G F V. Metallography principles and practice [M]. Ohio: ASM International, 1999.

[36] YUAN W, MISHRA R S, CARLSON B, VERMA R, MISHRA R K. Material flow and microstructural evolution during friction stir spot welding of AZ31 magnesium alloy [J]. Materials Science and Engineering A, 2012, 543: 200−209.

[37] SHANG Q, NI D R, XUE P, XIAO B L, MA Z Y. Evolution of local texture and its effect on mechanical properties and fracture behavior of friction stir welded joint of extruded Mg−3Al−1Zn alloy [J]. Materials Characterization, 2017, 128: 14−22.

[38] MIRONOV S, ONUMA T, SATO Y S, KOKAWA H. Microstructure evolution during friction-stir welding of AZ31 magnesium alloy [J]. Acta Materialia, 2015, 100: 301−312.

[39] TAKIGAWA Y, HONDA M, UESUGI T, HIGASHI K. Effect of initial grain size on dynamically recrystallized grain size in AZ31 magnesium alloy [J]. Materials Transactions, 2008, 49(9): 1979−1982.

[40] SELLARS C M, MCTEGART W J. On the mechanism of hot deformation [J]. Acta Metallurgica, 1966, 14(9): 1136−1138.

[41] WANG L X, FANG G., LEEFLANG M A, DUSZCZYK J, ZHOU J. Constitutive behavior and microstructure evolution of the as-extruded AE21 magnesium alloy during hot compression testing [J]. Journal of Alloys and Compounds, 2015, 622: 121−129.

[42] NAZEER F, LONG Jian-yu, YANG Zhe, LI Chuan. Superplastic deformation behavior of Mg alloys: A-review [J]. Journal of Magnesium and Alloys, 2022, 10(1): 97−109.

[43] HUA Zhen-ming, WANG Bing-yu, WANG Cheng, ZHANG Hong-min, DU Chun-feng, LI Yi-jia, ZHA Min, MA Pin-kui, YANG Zhi-zheng, WANG Hui-yuan. Solute segregation assisted superplasticity in a low-alloyed Mg−Zn−Ca−Sn−Mn alloy [J]. Materialia, 2020, 14: 100918.

[44] LANGDON T G. Grain boundary sliding revisited: Developments in sliding over four decades [J]. Journal of Materials Science, 2006, 41: 597−609.

多道次搅拌摩擦加工 Mg−3Zn−0.5Zr 合金的显微组织演变与热拉伸行为

王 佶[1,2]，付瑞东[1,3]，胡天祥[4]，李艺君[1,3]，刘 悦[1]，朱志华[2]，李世德[2]，许哲峰[1,3]

1. 燕山大学 亚稳材料制备技术与科学国家重点实验室，秦皇岛 066004；
2. 中信戴卡股份有限公司，秦皇岛 066004；
3. 燕山大学 材料科学与工程学院，秦皇岛 066004；
4. 首都航天机械公司，北京 100076

摘 要：系统研究单道次和多道次搅拌摩擦加工(FSP)后 ZK30 合金的显微组织和热拉伸行为。单道次搅拌摩擦加工(S-FSP)后，搅拌区(SZ)中的粗晶被细化至 1~2 μm，并呈现显著的基面织构。此外，第二相粒子发生碎裂、分散并部分溶解。多道次搅拌摩擦加工(M-FSP)提高了 ZK30 合金显微组织的均匀性，降低了搅拌区的织构强度差异，第二相粒子的比例降低了 50%。在应变速率低于 1×10^{-3} s^{-1} 和温度为 250~350 ℃时 S-FSP 和 M-FSP SZ 均表现出超塑性。S-FSP SZ 在 250 ℃和 1×10^{-4} s^{-1} 时的断裂伸长率为 390%，而 M-FSP SZ 在 350 ℃和 1×10^{-3} s^{-1} 时的断裂伸长率为 406%。对于 S-FSP，SZ 的超塑性变形主要由晶界滑移(GBS)和溶质拖曳机制协同作用，而对于 M-FSP，GBS 为其主要变形机制。

关键词：ZK30 合金；多道次搅拌摩擦加工；超塑性；显微组织；热拉伸行为

(Edited by Xiang-qun LI)